

Form-birefringent space-variant inhomogeneous medium element for shaping point-spread functions

Chia-Ho Tsai, Uriel Levy, Lin Pang, and Yeshaiahu Fainman

We experimentally characterize the properties of an element that generates a doughnutlike point-spread function by converting the linearly polarized incident field to radially or azimuthally polarized light utilizing space-variant inhomogeneous medium (SVIM) form-birefringent subwavelength structures. To fabricate the high-aspect-ratio SVIM structures, we developed a chemically assisted ion-beam-etching process that permits control of the fabricated form-birefringent structure profile to optimize the effect of birefringence and the impedance mismatch on the substrate-air interface. Fabricated elements perform efficient polarization conversion for incident angles as large as 30° , where the extinction ratio is found to be better than 4.5. The intensity distribution in the far field shows that our SVIM device generates a doughnut point-spread function that may prove useful for various applications. © 2006 Optical Society of America

OCIS codes: 220.4000, 230.5440, 260.5430.

1. Introduction

Radially and azimuthally polarized modes are known to be useful for various applications such as laser processing, tight focusing of light, and low-loss propagation in metal-clad fibers.^{1,2} Traditionally such polarization modes are obtained by the interference of two linearly polarized laser beams³ implemented with a bulky and complex optical system or by a space-variant twisted nematic liquid crystal,⁴ which requires a continuous power supply. Moreover the latter approach may not be possible to operate at high-power densities and outside the visible spectral range. Alternatively, polarization transformation can be performed by using form-birefringent elements implemented with subwavelength periodic structures etched into a high-refractive-index substrate material. Such artificially engineered inhomogeneous dielectrics typically exhibit higher birefringence than natural anisotropic materials and can be easily exploited to control the local properties of the optical field,^{5–10} enabling opportunities not available with

natural crystals. The application of such structures for the implementation of polarization-selective optical elements¹¹ demonstrates our ability to independently modulate the phase of orthogonally polarized optical fields in a space-variant manner. Recently, form birefringence has been further exploited to demonstrate radial and azimuthal polarization modes.^{12,13} Specifically, instead of the quarter-wave-plate approach,¹² the design of Ref. 13 uses a space-variant inhomogeneous medium (SVIM) with a half-wave plate approach to achieve higher conversion efficiency by effectively utilizing the aperture of the incident optical field. Moreover it operates with linear incident polarization, making it compatible with commonly used polarized laser sources.

In this paper we develop the technology for the microfabrication of the form-birefringent SVIM element for shaping applications of the point-spread function and experimentally investigate and optimize its optical properties, such as efficiency, impedance, and spatial-frequency response. In addition, we show experimentally that the impulse response of a radially and azimuthally polarized pupil results in a doughnut-shaped function. In Section 2 we present a brief review of the design concept of such elements to make the paper self-contained. In Section 3 we describe in detail the fabrication of subwavelength structures with a high aspect ratio and a controllable etch profile by using a chemically assisted ion-beam-etching (CAIBE) system, to our knowledge the first such comprehensive report presented for a CAIBE

The authors are with the University of California, San Diego, Department of Electrical and Computer Engineering, 9500 Gilman Drive, La Jolla, California 92093-0407. C.-H. Tsai's e-mail address is chiaho@ece.ucsd.edu.

Received 1 March 2005; revised 8 August 2005; accepted 30 August 2005; posted 2 September 2005 (Doc. ID 60163).

0003-6935/06/081777-08\$15.00/0

© 2006 Optical Society of America

system with a broad beam ion source.^{14–16} Moreover the profiles are evaluated for reduction of the reflection loss through adiabatic impedance matching between the substrate and the air. In Section 4 we present detailed experimental results for our SVIM element. In particular, we validate the generation of azimuthal polarization states for optical fields with an angular bandwidth in the range of $\pm 30^\circ$. We also validate the far-field distribution of the optical mode that is generated by the SVIM device, confirming experimentally the creation of a doughnut-shaped spot instead of a conventional Airy disk. This is an additional advantage of our approach compared with the quarter-wave-plate approach, where an additional spiral phase plate is needed to generate the doughnut beam. Moreover we experimentally compare the optical transmission through various subwavelength grating profiles, validating that a triangular profile allows higher transmission because it diminishes the Fresnel reflections by allowing adiabatic transition of the refractive index between the substrate–air interface, as predicted numerically.^{5,17} Finally, we present conclusions in Section 5.

2. Design

It is well known that form-birefringent subwavelength periodic structures can be used to engineer the polarization dispersion relation between the propagating TE- and TM-polarized optical fields.^{7,8} The form-birefringence effect is equivalent to what is observed in uniaxial anisotropic crystals but on a larger scale. The strength of form birefringence is determined mainly by the refractive index contrast of the constituent materials and by the duty cycle of the periodic structure. If the depth of the periodic structure is designed to introduce a π phase shift between the TE and the TM components, it acts as half-wave retardation plate, rotating the polarization angle of the incident linearly polarized light. By controlling the orientation of the form-birefringent structure, we can engineer the amount of rotation for the incident linearly polarized light in a space-variant manner, thereby creating any desired polarization distribution within the aperture of the incident linearly polarized field.

Next we briefly review the design concepts for our SVIM element, as previously described in Ref. 13. We then develop an analytic term for the polarization conversion efficiency for the plane wave and the Gaussian beam profile and compare it with the polarization conversion efficiency of the quarter-wave-plate approach.

In our design we consider an incident field propagating in the z direction and linearly polarized along the x axis [e.g., P_i in in Fig. 1(a)]. Our goal is to construct a beam that is linearly polarized in the radial (azimuthal) direction along the \hat{r} ($\hat{\theta}$) axis in the polar coordinate system (\hat{r} , $\hat{\theta}$); i.e., the polarization state of the output field P_o shown in Fig. 1(a) is oriented at an angle θ with respect to the x axis, as shown schematically in Fig. 1(b). Thus we need to create a half-wave

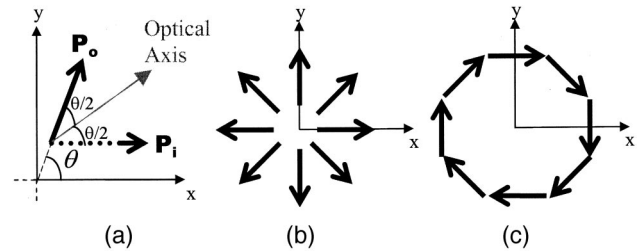


Fig. 1. Schematic diagram describing polarization transformation: (a) description of the geometry definitions, (b) definition of a radial polarization state, (c) definition of an azimuthal polarization state.

retardation plate with the principal axis oriented at an angle $\theta/2$ with respect to the x -polarized input field. The grating vector \mathbf{K}_g for achieving the space-variant polarization transformation along the \hat{r} axis needs to satisfy

$$\begin{aligned} \mathbf{K}_g &= \frac{2\pi}{\Lambda_g(r, \theta)} \left[\cos\left(\frac{\theta}{2}\right)\hat{r} - \sin\left(\frac{\theta}{2}\right)\hat{\theta} \right] \\ &= \frac{2\pi}{a_0\sqrt{r}} \left[\cos\left(\frac{\theta}{2}\right)\hat{r} - \sin\left(\frac{\theta}{2}\right)\hat{\theta} \right], \end{aligned} \quad (1)$$

where $\Lambda_g(r, \theta)$ is the local period of the grating and a_0 is a constant that is chosen to meet the fabrication constraints and aperture dimension requirements. The second equality was obtained by assuming a radial dependency of the grating period, i.e., $\Lambda_g(r, \theta) = \Lambda_g(r)$, and applying the continuity condition $\nabla \times \mathbf{K}_g = 0$. It can be shown that such a grating can also produce an azimuthal polarization state [shown schematically in Fig. 1(c)] if it is rotated by 90° with respect to the x axis. From Eq. (1) it is evident that the period of the SVIM is proportional to $r^{1/2}$; i.e., the period of the element becomes infinitesimally small as we approach the central portion of the element. Such a small period cannot be supported by the fabrication process, leading to a hole in the center of the element. However, with our approach the radius of the hole is much smaller than that of the quarter-wave-plate approach (since for that approach the period is linearly increasing with r). Thus we anticipate a significant increase in the overall conversion efficiency.

We designed the SVIM element to operate at a wavelength of $10.6 \mu\text{m}$ and to be realized by a GaAs subwavelength grating (with a refractive index of 3.13 at this wavelength). To ease the fabrication process we restrict the minimal period to $\Lambda_{g,\text{min}} = 2 \mu\text{m}$, and, to avoid internal diffraction within the substrate and to reduce dispersion,¹⁸ we set the maximal period to be $\Lambda_{g,\text{max}} = 3.05 \mu\text{m}$. By designing the outer radius of the device to be 7 mm, we obtain $a_0 = 3.05/(7)^{1/2} (\mu\text{m}/\text{mm}^{1/2})$ with the corresponding inner radius, $r_{\text{min}} = (2/a_0)^2 = 3 \text{ mm}$. The required etching depth to achieve the desired π phase shift between the TE and the TM polarization components was estimated from the rigorous coupled-wave anal-

ysis¹⁹ (RCWA) to be 6 μm (assuming a rectangular profile with a duty cycle of 50%).

The unutilized area of our SVIM element owing to the central hole is ~18% of the total area. For comparison, by using the design approach of the quarter-wave plate with the same period restrictions, one obtains an ~43% unutilized area due to the central hole, significantly reducing polarization conversion efficiency. Note that the reduction of the unutilized area is in general true since with our design the ratio of the inner to the outer radius is

$$r_{in} = r_{out}(\Lambda_{g,min}/\Lambda_{g,max})^2, \quad (2)$$

whereas the quarter-wave-plate approach yields

$$r_{in} = r_{out}(\Lambda_{g,min}/\Lambda_{g,max}). \quad (3)$$

The significance of reducing the central hole becomes even more pronounced if we consider a Gaussian beam illumination, since most of the energy is now concentrated in the central portion of the element. For Gaussian beam illumination the conversion efficiency is given by

$$\begin{aligned} \eta &= \frac{2\pi \int_{r_{in}}^{r_{out}} \exp\left[-2\left(\frac{r'}{\omega}\right)^2\right] r' dr'}{2\pi \int_0^{r_{out}} \exp\left[-2\left(\frac{r'}{\omega}\right)^2\right] r' dr'} \\ &= \frac{\exp\left[-2\left(\frac{r_{in}}{\omega}\right)^2\right] - \exp\left[-2\left(\frac{r_{out}}{\omega}\right)^2\right]}{1 - \exp\left[-2\left(\frac{r_{out}}{\omega}\right)^2\right]}, \end{aligned} \quad (4)$$

where ω is the beam half-width. By using Eqs. (2) and (3), we obtain

$$\eta_1 = \frac{\exp\left[-2\left(\frac{r_{out}}{\omega}\right)^2 \left(\frac{\Lambda_{g,min}}{\Lambda_{g,max}}\right)^4\right] - \exp\left[-2\left(\frac{r_{out}}{\omega}\right)^2\right]}{1 - \exp\left[-2\left(\frac{r_{out}}{\omega}\right)^2\right]}, \quad (5)$$

$$\eta_2 = \frac{\exp\left[-2\left(\frac{r_{out}}{\omega}\right)^2 \left(\frac{\Lambda_{g,min}}{\Lambda_{g,max}}\right)^2\right] - \exp\left[-2\left(\frac{r_{out}}{\omega}\right)^2\right]}{1 - \exp\left[-2\left(\frac{r_{out}}{\omega}\right)^2\right]}, \quad (6)$$

where $\eta_{1,2}$ stands for our approach and the quarter-wave-plate approach, respectively. The predicted conversion efficiencies in Fig. 2 show the advantage of our approach in achieving much higher efficiencies at smaller values of ω . As the value of ω increases, both approaches reach their corresponding asymptotic values derived for plane-wave illumination.

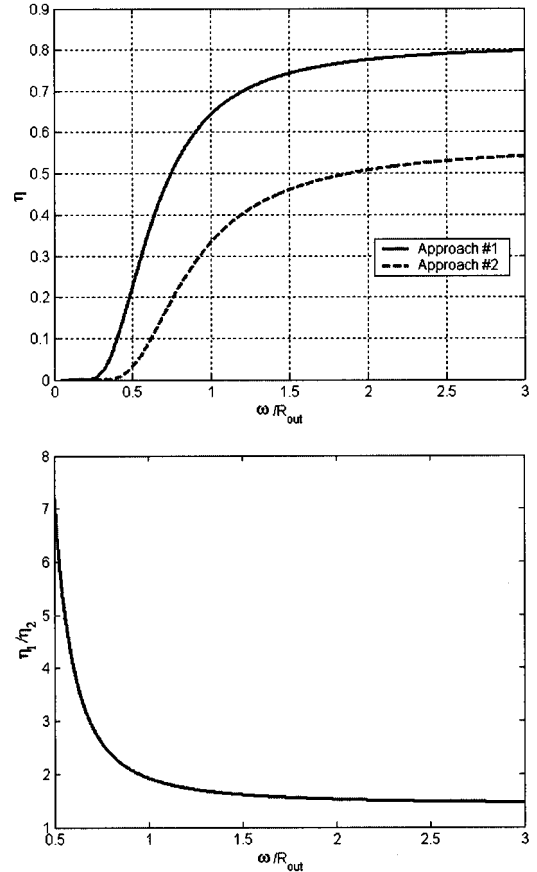


Fig. 2. Top, polarization conversion efficiency versus normalized Gaussian beam width: 1, half-wave-plate approach; 2, quarter-wave-plate approach. Both values approach the asymptotic limit of plane-wave illumination as the normalized beam width increases. Bottom, ratio of efficiency between the two approaches versus the normalized Gaussian beam width. The ratio increases with a decrease in the normalized Gaussian beam width.

3. Fabrication Process

To fabricate the device, the GaAs substrate is coated with antireflection layers at the back side to reduce the insertion loss and to eliminate the multiple reflection within the sample, which may interfere with the desired polarization dispersion relation. The front side of the substrate is patterned with BPRS-100 photoresist as a dry etch mask by standard photolithography. To transfer the mask pattern into the GaAs substrate, we choose CAIBE, which provides a high-aspect-ratio etch profile to meet the design specifications with a minimal feature size of ~1 μm and an etch depth of ~6 μm. Unlike reactive ion beam etching (RIE), the CAIBE process provides independent control of the physical bombardment and the chemical etch reaction.^{14–16,20–24} This is especially important when a single layer of photoresist is used as the dry etch mask for deep profiles with small feature sizes, because one can take advantage of its chemical resistance to reactive gases to eliminate the necessity for further pattern transfer processes.²²

Previously, the anisotropy of high-aspect-ratio profiles has been characterized for samples fabricated

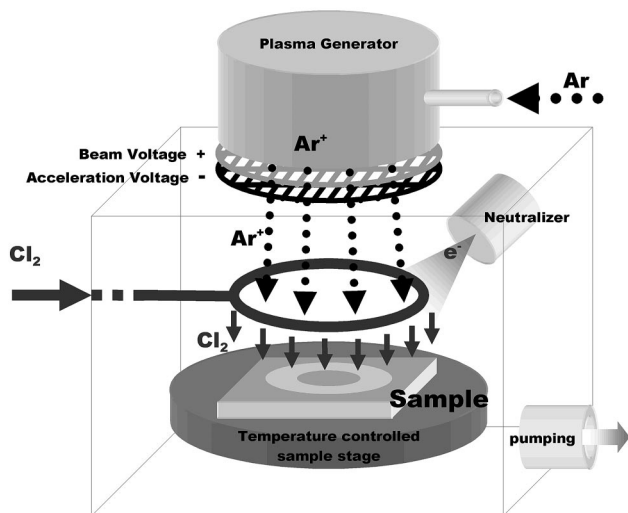


Fig. 3. Chamber diagram of a CAIBE system. The physical etching mechanism provided by argon-ion bombardment and the chemical etching mechanism provided by the Cl_2 reaction can be controlled independently.

with a small-ion-source²⁴ CAIBE system as well as for samples fabricated with a broad-beam-source¹⁶ RIBE system. However, the anisotropy of form birefringent structures fabricated with a broad-beam-source CAIBE system has not yet been reported. The latter is of appreciable interest because of its suitability for mass production. In this project we utilize a 12 cm broad beam source for our CAIBE setup and investigate the profile dependence on etching parameters.

The setup of our CAIBE system is shown schematically in Fig. 3. The chemical reaction mechanism is controlled by the flow rate of the reactive gas (Cl_2 in our case) and the sample temperature, whereas the physical bombardment mechanism is controlled by the flow rate of the inert gas (argon in our case), the amount of generated ions, the ion beam energy, and the beam collimation, which can be adjusted with the beam and acceleration voltages (V_b and V_a) applied on the grids. The grid-to-sample distance is ~ 45 cm. The chamber pressure is controlled with the flow rates of the processing gases, and it can affect the chemical reaction rate as well as the mean free path of the gas molecules. A neutralizer is used to prevent ionic charging on the sample surface. The base pressure of the chamber is kept at 1×10^{-7} Torr.

With an overpowered physical bombardment in the CAIBE process the ions tend to cause surface damage, meanwhile the etch mask erodes considerably. Conversely, an insufficient physical bombardment results in significant surface redeposition and increases the roughness of the sample surface. For example, in our test samples Fig. 4(a) shows an overcut etch that is the result of mask erosion due to excess physical bombardment, and Fig. 4(b) shows a structure with significant surface roughness due to excess chemical reactions. Therefore a balanced process is usually necessary to fabricate smooth and accurate profiles

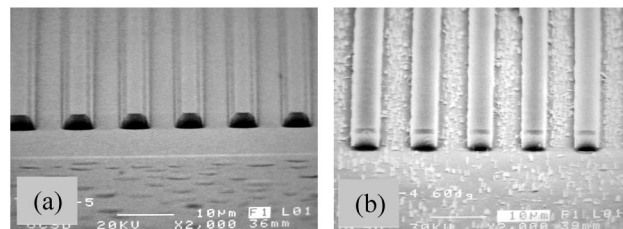


Fig. 4. SEM pictures of the testing etched sample profiles demonstrating the effects of excess physical or chemical mechanisms. (a) Excess physical bombardment eroding the mask considerably and causing overcut etch profiles. When overpowered, it may also cause surface damage to the sample. (b) Excess chemical reaction enhancing surface redeposition randomly all over the sample and increasing the surface roughness. Strong redeposition can dominate and inhibit the etching process.

with high-aspect-ratio structures that maintain the original profile of the etch mask. For this particular case we optimize the balanced recipe with $V_b = 600$ V and $V_a = 500$ V at 20°C and fabricate a device with a rectangular 6:1 aspect-ratio etch profile [Fig. 5(a)]. The proportion of Cl_2 to Ar is kept at 26:17 in the chamber with the Ar^+ plasma generation power at 95 W.

Although a rectangular profile is ideal for achieving large phase retardation, it gives rise to an undesired Fresnel reflection at the grating-air boundary. The effect can be minimized if the grating structure has an etch profile of trapezoidal or triangular shape.^{5,17} To fabricate a high-aspect-ratio structure with the overcut effect as shown in Fig. 4(a), we deliberately increase the number of argon ions by setting Ar^+ generation power to 100 W with a higher kinetic energy level at $V_b = 700$ V. To maintain the selectivity of the etching process, the proportion of Cl_2 to Ar is set to 30:17. Meanwhile, when $V_b = 700$ V and $V_a = 500$ V are set, the collimation of the ion beam provides the sufficient lateral erosion rate of the mask. The adjustment is well managed so that the surface damage is minimized and the etch mask survives along the process, resulting in a deep, triangular etch profile [Fig. 5(b)]. To summarize, we have developed a dry etching process to tailor high-aspect-

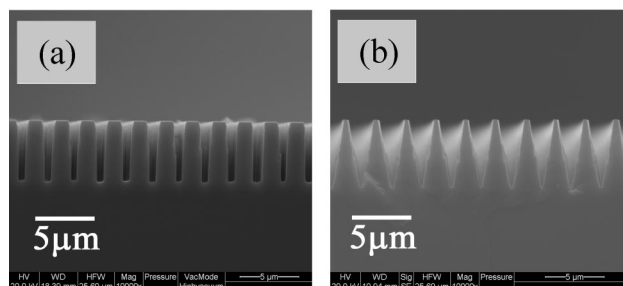


Fig. 5. SEM pictures of the cross sections of the etched sample profiles. The profile can be controlled with a degree of collimation of the ion beam: (a) Balanced recipe results in a rectangular etch profile; (b) recipe with extra lateral physical bombardment enhancing the mask erosion sideways, resulting in a triangular etch profile.

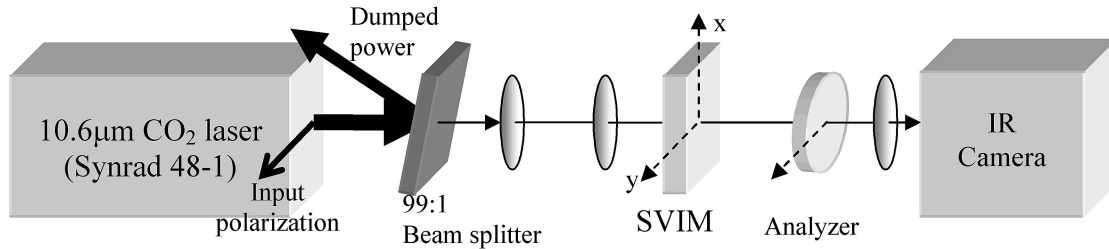


Fig. 6. Optical setup for the characterization of polarization conversion. A horizontally linear polarized beam retrieved from a CO₂ laser is expanded and collimated to cover the whole SVIM device. To measure the polarization states of the output, the image for analysis is acquired on the IR camera after a horizontally polarized analyzer.

ratio profiles in GaAs so that the trade-off between phase retardation and Fresnel reflection can be precisely controlled. Note that to render a triangular etch profile the V_b and V_a are set for a less divergent beam. This trend of anisotropy dependency is very different from a CAIBE system with a small ion source²⁴ but relatively close to a RIBE system with a broad beam source.¹⁶

4. Experimental Characterization Results

The fabricated form birefringent elements have been characterized experimentally to validate four features that we study in this paper. For all these experiments we use a linearly polarized beam, derived from a single-mode CO₂ laser at a wavelength of 10.6 μm. The input beam is expanded and collimated to cover the entire form-birefringent SVIM device aperture.

For the first validation experiment on generating a radial (azimuthal) polarization state the polarization of the incident beam aligned parallel to the $x(y)$ axis of the SVIM, producing a radial (azimuthal) polarization state. These experiments are conducted to validate that the newly fabricated element with variable grating profiles perform similarly to those validated in Ref. 13 and are not affected by the shape of the profile studied below. The output beam is transmitted through an analyzer converting polarization modulation of the wavefront into amplitude modulation. The output of the analyzer is then imaged onto an IR camera for measurement and further analysis. The optical setup is shown schematically in Fig. 6. The intensity distribution of the image detected by the IR camera is then used to verify the polarization conversion of the SVIM. To reduce the effect of lateral quantization noise due to the limited spatial resolution of the camera, we performed integration of the obtained intensity values along the radial axis at each angle θ . An example of the generation of an azimuthally polarized beam is shown in Fig. 7, where the normalized intensity is compared with the theoretical curve ($\sin^2 \theta$). It is evident that the experimental result fits the theoretical prediction well. Notice that the relatively low polarization contrast of $\sim 10:1$ is probably due to a slight discrepancy of the fabricated grating profile from the ideal profile. This result also agrees with that in the previous publication.¹³

In the second experiment we validate the expected

invariance of the linear to the azimuthal polarization converter to beams with varying incidence angles to enable operation with wide angular bandwidth signals in support of imaging applications. For this experiment we tilt the SVIM element with respect to the vertical axis and estimate its performance as a function of the angle of incidence. The results in Fig. 8 indicate that significant polarization conversion exists even for an incident angle of 30°, where the extinction ratio was estimated to be higher than 4.5 (notice that the fringes are caused by the backreflection of the imaging lenses of the IR camera). Therefore we believe that the SVIM device can also be integrated with imaging systems possessing relatively high numerical apertures. The observed elliptic shape of the image for higher incidence angles is due to the projection of the tilted device on the imaging plane. In realistic applications, where the beam is tilted rather than the device, this elliptic shape is eliminated.

In the third experiment we validate that the expected doughnutlike point-spread function is pro-

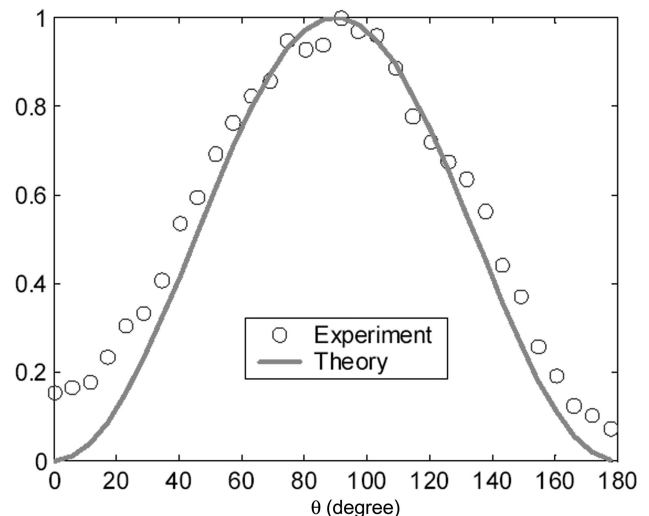


Fig. 7. Angular dependence of normalized transmitted intensity after the polarization analyzer, where θ is the angle to the horizontal, linearly polarized input. The experimental data are then obtained by digital integration across the radial coordinate of the image obtained with the setup in Fig. 6. The result agrees with the theoretical curve.

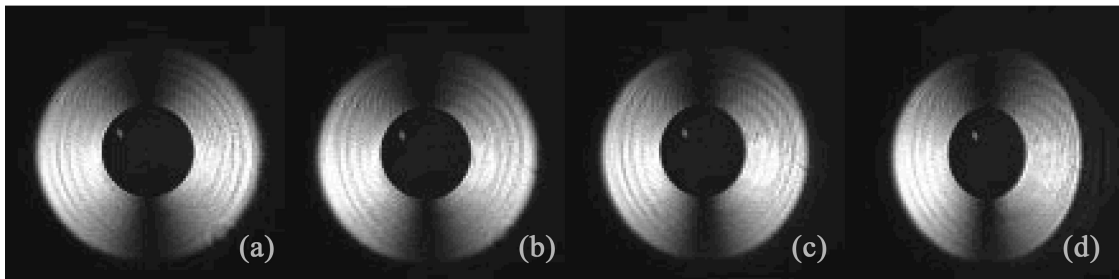


Fig. 8. Experimentally obtained image showing polarization conversion for various incident angles. A crossed analyzer was used to convert the polarization transformation into amplitude modulation: (a) 0°, (b) 10°, (c) 20°, (d) 30°.

duced by our SVIM element. For this experiment we removed the polarization analyzer in the system shown in Fig. 6 and used a converging illumination beam that produces the far-field distribution in the focal plane of the lens, located ~ 80 cm behind the SVIM element. The focal plane was then imaged onto the IR camera with a magnification ratio of ~ 2 . Horizontal cross sections of the calculated and the measured optical field distributions are in Fig. 9, while the inset corresponds to the entire far-field distribution as captured by the IR camera. The doughnut beam obtained is clearly observed, and the experimental result shows good agreement with the theoretical prediction. Note that the doughnut beam was obtained with direct laser illumination, whereas the quarter-wave-plate approach requires an additional spiral phase compensation plate, making that approach more cumbersome.

Finally we investigate the effect of the etch profile on the substrate–air interface. For this experiment we illuminated two different sets of samples at various regions with a narrow polarized beam (~ 1 mm in diameter) to measure the transmitted power. The transmittance for each sample is obtained by normalization with respect to the input power. In Table 1 we show the two sets of samples with triangular (A, B) and rectangular (C, D) etch profiles. Each set has two

samples with a slightly different duty cycle. For comparison the transmitted power is measured for each sample at the regions defined as TE ($\phi = 0$), TM ($\phi = \pi/2$), and 45° ($\phi = \pi/4$) within the SVIM and the substrate outside the SVIM, where ϕ is the angle of the local grating groove orientation with respect to the input polarization. In the TE and the TM regions the field distribution in the SVIM is similar to the TE and the TM modes defined in Ref. 5. For all four samples the transmission of the TE mode is slightly lower than (if not equal to) that of the TM mode. This is probably from the effect of the relatively higher effective index of the TE mode, making the local index of the SVIM slightly closer to the GaAs substrate compared with the TM mode. As expected, we also note that the transmission values in the 45° region for each of the samples usually fall between the TE and the TM values. In Table 1 we show that the two samples with triangular etch profiles provide significantly higher transmittance than those with rectangular profiles. This is due to the adiabatic transition from the index substrate to that of the air. The trend agrees well with the RCWA simulation results (see Table 1), where we utilize a $2 \mu\text{m}$ period infinite grating structure for each of the samples with profiles estimated from the cross sections of the scanning-electron-microscopy (SEM) images. Despite the minor discrepancies that are expected from the space-variant periodicity and scattering loss of the actual device, the simulation results agree well with our measurements. From the results it is evident that the triangular profile design significantly enhances the transmittance of the component. This trend also agrees with the previously reported theoretical simulations.^{5,17} Although the discussions above focus on only the design depicted in Section 2, note that similar fabrication considerations can be applied to the alternative design described in Ref. 13, where conversion efficiency can be further improved.

5. Conclusions

We experimentally characterize the properties of an optical element that generates a doughnutlike point-spread function by converting the linearly polarized incident field to radially or azimuthally polarized light utilizing SVIM form-birefringent subwavelength structures. The device is designed to locally introduce a π phase shift between the TE and the TM

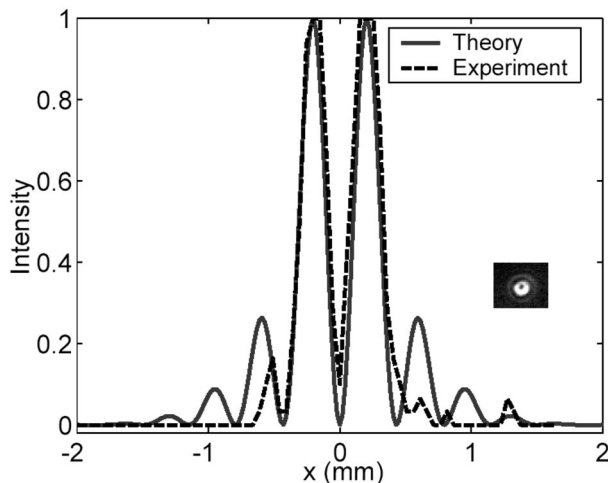
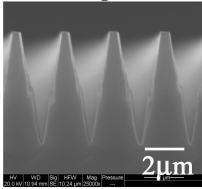
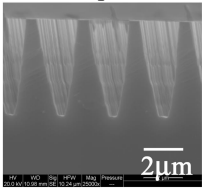
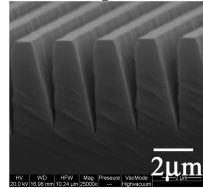
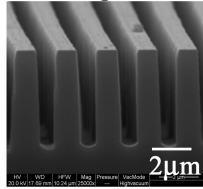


Fig. 9. Cross sections of the far-field distributions of the SVIM element.

Table 1. Measured Transmission on Four Different Samples over Different Regions^a

| | Sample A | Sample B | Sample C | Sample D |
|---|---|---|--|---|
| |  |  |  |  |
| | (%) | (%) | (%) | (%) |
| Air | 100 | 100 | 100 | 100 |
| Substrate | 72 | 72 | 71 | 70 |
| TE | 91 | 97 | 78 | 80 |
| 45° | 94 | 96 | 83 | 81 |
| TM | 96 | 97 | 86 | 81 |
| Filling factor (top-bottom) estimated for RCWA | 15-90 | 20-85 | 40-100 | 50-60 |
| TE (RCWA) | 95 | 92 | 85 | 86 |
| TM (RCWA) | 99 | 98 | 99 | 95 |

^aTE/TM represents the input signal with the electric field parallel/perpendicular to the subwavelength structures, respectively, and 45° represents somewhere between. Compared with the transmission to the substrate, which is the area without patterns, this shows that the transmission is enhanced where there is a subwavelength structure. Meanwhile the samples with triangular profiles (Samples A and B) in general exhibit higher transmission compared with those with rectangular profiles (Samples C and D). The triangular profile of the subwavelength structures therefore serves as a better antireflection coating at the sample surface. The trend agrees with the RCWA theoretical results shown that are simulated with 2 μm period gratings with similar profiles.

input polarization components, thereby converting the incident linearly polarized light into the desired radial or azimuthal distribution. To fabricate the high-aspect-ratio deep structures for operation at a wavelength of 10.6 μm, we have developed a CAIBE process that enables control of the fabricated form-birefringent structure profile to optimize the effect of birefringence and the impedance mismatch on the substrate–air interface, and the results show higher transmission values with triangular profiles since these structures provide adiabatic transition at the substrate–air interface. Fabricated elements perform efficient polarization conversion for incident angles of as many as 30°, where the extinction ratio was found to be better than 4.5. Finally the intensity distribution in the far field shows that our SVIM device generates a doughnut point-spread function, which may prove useful in various applications.

This research is supported in part by the U.S. Air Force Office of Scientific Research, the National Science Foundation, the Defense Advanced Research Projects Agency, and the Space and Naval Warfare Systems Command.

References

- V. G. Niziev and V. Nesterov, "Influence of beam polarization on laser cutting efficiency," *J. Phys. D* **32**, 1455–1461 (1999).
- S. Quabis, R. Dron, M. Eberler, O. Glockl, and G. Leuchs, "Focusing light to a tighter spot," *Opt. Commun.* **179**, 1–7 (2000).
- S. C. Tidwell, D. H. Ford, and W. D. Kimura, "Generating radially polarized beams interferometrically," *Appl. Opt.* **29**, 2234–2239 (1990).
- M. Stalder and M. Schadt, "Linearly polarized light with axial symmetry generated by liquid-crystal polarization converters," *Opt. Lett.* **21**, 1948–1950 (1996).
- I. Richter, P. C. Sun, F. Xu, and Y. Fainman, "Design considerations of form birefringent microstructures," *Appl. Opt.* **34**, 2421–2429 (1995).
- F. Xu, R. Tyan, P. C. Sun, C. Cheng, A. Scherer, and Y. Fainman, "Fabrication, modeling, and characterization of form-birefringent nanostructures," *Opt. Lett.* **20**, 2457–2459 (1995).
- W. Nakagawa, R. Tyan, P. C. Sun, and Y. Fainman, "Ultra-short pulse propagation in near-field periodic diffractive structures by use of rigorous coupled-wave analysis," *J. Opt. Soc. Am. A* **18**, 1072–1081 (2001).
- C. Gu and P. Yeh, "Form birefringence dispersion in periodic layered media," *Opt. Lett.* **21**, 504–506 (1996).
- S. Y. Chou and W. Deng, "Subwavelength amorphous silicon transmission gratings and applications in polarizers and wave plates," *Appl. Phys. Lett.* **67**, 742–744 (1995).
- G. P. Nordin and P. C. Deguzman, "Broadband form birefringent quarter-wave plate for the mid-infrared wavelength region," *Opt. Express* **5**, 163–168 (1999).
- F. Xu, J. Ford, and Y. Fainman, "Single-substrate birefringent computer-generated holograms," *Opt. Lett.* **21**, 516–518 (1996).
- Z. Bomzon, G. Biener, V. Kleiner, and E. Hasman, "Radially and azimuthally polarized beams generated by space-variant dielectric subwavelength gratings," *Opt. Lett.* **27**, 285–287 (2002).
- U. Levy, C. H. Tsai, L. Pang, and Y. Fainman, "Engineering space-variant inhomogeneous media for polarization control," *Opt. Lett.* **29**, 1718–1720 (2004).

14. J. D. Chinn, I. Adesida, and E. D. Wolf, "Profile formation in CAIBE," *Solid State Technol.* **27**, 123–129 (1984).
15. K. R. Milkove, J. A. Coffin, and C. Dziobkowski, "Effects of argon addition to a platinum dry etch process," *J. Vac. Sci. Technol. A* **16**, 1483–1488 (1998).
16. W. J. Zubrzycki, G. A. Vawter, and J. R. Wendt, "High-aspect-ratio nanophotonic components fabricated by Cl_2 reactive ion beam etching," *J. Vac. Sci. Technol. B* **17**, 2740–2744 (1999).
17. D. H. Raguin and G. M. Morris, "Antireflection structured surfaces for the infrared spectral region," *Appl. Opt.* **32**, 1154–1167 (1993).
18. U. Levy and Y. Fainman, "Dispersion properties of inhomogeneous nanostructures," *J. Opt. Soc. Am.* **21**, 881–889 (2004).
19. M. G. Moharam and T. K. Gaylord, "Diffraction analysis of dielectric surface-relief gratings," *J. Opt. Soc. Am.* **72**, 1385–1392 (1982).
20. I. Adesida, A. T. Ping, C. Youtsey, T. Dow, M. Asif Khan, D. T. Olson, and J. N. Kuznia, "Characteristics of chemically assisted ion beam etching," *Appl. Phys. Lett.* **65**, 889–891 (1994).
21. A. Scherer, J. L. Jewell, Y. H. Lee, J. P. Harbison, and L. T. Florez, "Fabrication of microlasers and microresonator optical switches," *Appl. Phys. Lett.* **55**, 2724–2726 (1989).
22. M. Chabloz, Y. Sakai, T. Matsuura, and K. Tsutsumi, "Improvement of sidewall roughness in deep silicon etching," *Microsyst. Technol.* **6**, 86–89 (2000).
23. C. C. Cheng and A. Scherer, "Fabrication of photonic band-gap crystals," *J. Vac. Sci. Technol. B* **13**, 2696–2700 (1995).
24. G. A. Lincoln, M. W. Geis, S. Pang, and N. N. Efremow, "Large area ion-beam-assisted etching of GaAs with high etch rates and controlled anisotropy," *J. Vac. Sci. Technol. B* **1**, 1043–1046 (1983).